

Quantitative morphology of epithelial folds

Supplementary information

Nick Štorgel,^{†‡} Matej Krajnc,[†] Polona Mrak,[§] Jasna Štrus,[§] and Primož Ziherl^{†‡¶}

[†]Jožef Stefan Institute, Jamova 39, SI-1000 Ljubljana, Slovenia

[‡]Faculty of Mathematics and Physics, University of Ljubljana, Jadranska 19, SI-1000 Ljubljana, Slovenia

[§]Biotechnical Faculty, University of Ljubljana, Jamnikarjeva 101, SI-1000 Ljubljana, Slovenia and

[¶]Erwin Schrödinger International Institute for Mathematical Physics,

University of Vienna, Boltzmanngasse 9, A-1090 Vienna, Austria

I. MECHANICAL BASIS OF FOLD FORMATION

To illustrate the various mechanisms that determine the equilibrium shape of tissues within our model (tissue lateral tension, tissue differential tension, bending rigidity of the basement membrane, cell-cell repulsion, and confinement by the stroma), it is instructive to study a free-standing 2D epithelium supported by the basement membrane alone. Unlike our main model, here the substrate enforcing a global planar geometry is absent, and all cells adopt the same shape. Thus the curvature of the chain of cells is constant but generally nonzero such that the model tissue may be either flat or curved, depending on the values of parameters.

In the dimensionless form of our discrete model (Eq. 3 of the main text), the energy of a cell attached to the basement membrane can be written as

$$w = \alpha l_a + \beta l_b + \frac{1}{2} l_l + \frac{\kappa}{2} c_{\text{bend}}^2 l_b, \quad (1)$$

where l_a , l_b , and l_l are the lengths of apical, basal, and lateral cell sides, respectively, and c_{bend} is the curvature of the basement membrane. The lengths l_a , l_b , and l_l are not independent because cells are incompressible and so their area is constant and normalized to 1. Instead of using these three lengths, it is convenient to parametrize cell shape by midline curvature c and height l (also representing tissue thickness) as two independent parameters (Fig. S1); cell width is then determined by the fixed-area constraint. Within this parametrization the dimensionless energy of a single cell in a free-standing epithelium–basement membrane system reads

$$w = \frac{\alpha + \beta}{l} + \frac{(\alpha - \beta)c}{2} + l \sqrt{1 + \left(\frac{c}{2l}\right)^2} + \frac{\kappa c^2}{l(2 - cl)}. \quad (2)$$

At any given reduced apical tension, basal tension, and basement membrane bending modulus (α , β , and κ , respectively) the optimal, minimal-energy cell shape is found by solving $\partial w/\partial c = 0$, $\partial w/\partial l = 0$, which generally has to be done numerically.

Based on rectangular cells, our model is an approximation as the exact shape of a droplet-like cell carrying surface energy alone is curved like in a cluster of soap bubbles. By disregarding the curvature of the sides, we approximate the force balance at the cell-cell contact.

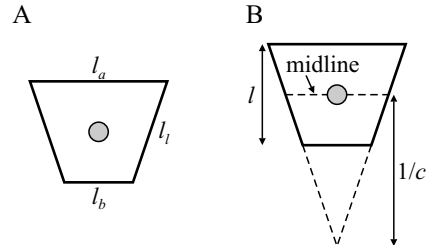


Fig. S1. Two equivalent parametrizations of cell shape: Edge-length representation based on (l_a, l_b, l_l) together with the incompressibility constraint $A = 1$ (panel A) or curvature-height representation based on (c, l) (panel B).

Nonetheless, assuming that cell sides are flat is reasonable because our model (Eq. 1 of the main text) is to be viewed as an effective description designed so as to reproduce the overall behavior of epithelial cells, which are rarely curved, and the flat-side constraint is a part of the phenomenological framework.

Below we analyze the influence of model parameters α , β , and κ on the minimal-energy shape of the tissue.

A. Tissue lateral tension

Cell width-to-height ratio is governed by the lateral tension defined by $\alpha + \beta$. In case of a flat epithelium where $l_a = l_b$ and thus $c = 0$ cell proportions can be calculated straightforwardly. The energy per cell is

$$w_{\text{flat}} = \frac{\alpha + \beta}{l} + l, \quad (3)$$

and the optimal cell height is determined by $\partial w_{\text{flat}}/\partial l = 0$. By taking into account the incompressibility constraint $A = l_a l = 1$, we find

$$\frac{l_a}{l} = \frac{1}{\alpha + \beta}. \quad (4)$$

$l_a/l \ll 1$ and $l_a/l \gg 1$ correspond to a columnar and a squamous epithelium, respectively; in a cuboidal epithelium $l_a/l \approx 1$ (Fig. S2A). Cell width-to-height ratio l_a/l also depends on tissue differential tension $\alpha - \beta$ but this effect is subdominant compared to the interplay of tissue lateral tension $\alpha + \beta$ and incompressibility leading

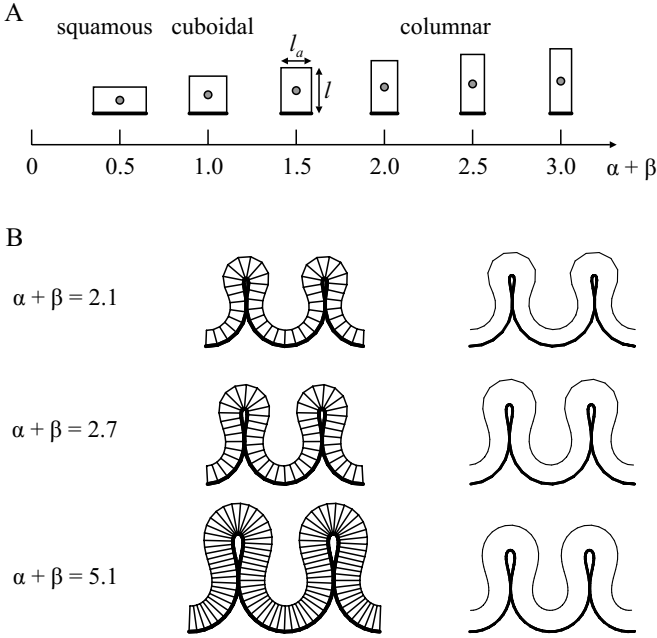


Fig. S2. Equilibrium cell shapes vs. reduced tissue lateral tension $\alpha + \beta$ at vanishing differential tension $\alpha - \beta$ (panel A). At small $\alpha + \beta \ll 1$ the cell is flattened, i.e., squamous, at $\alpha + \beta = 1$ it is isometric, i.e., cuboidal, whereas at large $\alpha + \beta \gg 1$ it is tall, i.e., columnar. Three examples of evaginated folds with identical differential tension of $\alpha - \beta = 1.5$ and bending rigidity $\kappa = 0.001$ and different tissue lateral tensions $\alpha + \beta$ (panel B, left column). In the right column, the folds are scaled such that their wavelengths are identical, which emphasizes that their shapes are very similar.

to Eq. 4, which is a rather good estimate of l_a/l for all nontrivial folded structures studied here.

Cell width-to-height ratio l_a/l also affects the equilibrium number of cells in a waveform. In Ref. [28] of the main text we showed that the contour of tissue midline is mainly determined by the differential tension $\alpha - \beta$ and that tissue lateral tension $\alpha + \beta$ only controls the number of cells in the waveform through the width-to-height ratio; the larger the tissue lateral tension the larger the number of cells in the waveform. The three evaginated folds plotted in Fig. S2 have identical differential tension $\alpha - \beta = 1.5$ and bending modulus $\kappa = 0.001$ but they differ in the value of α ($\alpha = 0.3$, $\alpha = 0.6$, and $\alpha = 1.8$) and thus in the value of tissue lateral tension ($\alpha + \beta = 2.1$, 2.7 , and 5.1 , respectively). As $\alpha + \beta$ is increased, the number of cells in a waveform clearly increases too whereas the cell width-to-height ratio decreases (Fig. S2B, left column). Nonetheless, the outline of the folds does not change significantly. This is best appreciated by comparing the thick line of fold shapes in the right column of Fig. S2B scaled such that their wavelengths are the same.

At a very low lateral tension $\alpha + \beta$ where the tissue is squamous, α and $\beta > 0$ must be small themselves and so the differential tension is small too. As a result, the tissue is flat. This means that in our model where we

approximate cells as quadrilaterals with flat edges, we cannot obtain nontrivial squamous epithelia.

B. Apico-basal differential tension

In our model, formation of nontrivial epithelial shapes is driven by the interplay between the spontaneous curvature, determined mainly by the tissue differential tension, and periodic boundary conditions imposed by the implicit (fluid-like) stroma. In case of vanishing basement membrane bending modulus ($\kappa = 0$) the spontaneous curvature of cells describing their preferred shape can be calculated analytically and reads

$$c_0 = -\frac{2\sqrt{\alpha + \beta}(\alpha - \beta)}{[1 - (\alpha - \beta)^2]^{3/4}}. \quad (5)$$

c_0 grows with the magnitude of the differential tension $\alpha - \beta$, transforming the rectangular shape into a trapezoid and then into a triangle at a threshold of

$$(\alpha - \beta)_{th} = \frac{1}{2} \left[\alpha + \beta - \sqrt{4 + (\alpha + \beta)^2} \right]. \quad (6)$$

At $|\alpha - \beta| = (\alpha - \beta)_{th}$ cells are either apically (if $\alpha > \beta$) or basally constricted (if $\alpha < \beta$) and beyond the threshold value cell shape no longer changes with $\alpha - \beta$.

Our numerical results show that the differential tension $\alpha - \beta$ not only determines the tissue spontaneous curvature but also the amplitude of thickness modulation δl in epithelial folds. Here δl is defined as the difference of groove and crest tissue thickness (Fig. 1B of the main text). Figure S3 shows the relative thickness modulation $\delta l/l_0$ in absence of basement membrane ($\kappa = 0$); here $l_0 = \sqrt{\alpha + \beta}$ is the leading-order estimate of tissue thickness. In the flat epithelium at $\alpha - \beta \approx 1.4$, $\delta l/l_0 = 0$ but in the folded epithelium it increases approximately as $\delta l/l_0 \propto (\alpha - \beta)/\sqrt{\alpha + \beta}$. Apart from the agreement

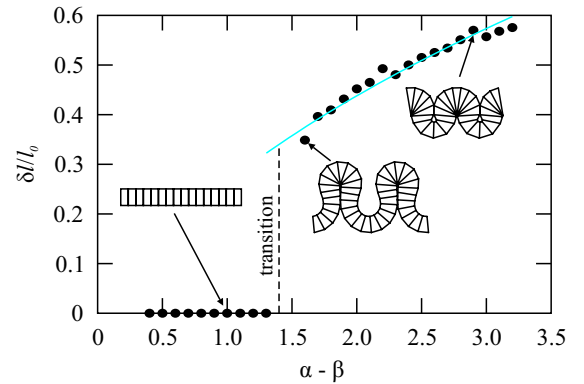


Fig. S3. Relative tissue thickness modulation $\delta l/l_0$ vs. reduced differential tension $\alpha - \beta$ in a model epithelium at fixed $\alpha = 0.6$ and without the basement membrane ($\kappa = 0$). Insets illustrate a few typical waveforms and in the fold domain at $\alpha - \beta > 1.4$, $\delta l/l_0 \propto (\alpha - \beta)/\sqrt{\alpha + \beta}$ (cyan line).

with this simple fit, note the large magnitude of relative thickness modulation reaching $\approx 60\%$ in the tissues shown here. We stress that as the fold shape itself saturates as $\alpha - \beta$ is increased further (Ref. [28] of the main text) so does $\delta l/l_0$, implying that the above approximate formula cannot be generally applicable.

Our results suggest that tissue thickness modulation does not depend very dramatically on the other two parameters of the model, i.e., κ and $\alpha + \beta$. Moreover, they show that for $\alpha > \beta$ and $\alpha < \beta$ tissue thickness is largest in the part of the waveform containing apically or basally constricted cells, respectively.

C. Bending rigidity of basement membrane

As the basement membrane bending modulus κ is increased, the contour of any folded epithelium is somewhat straightened out as seen in Fig. 1D, E of the main text. Unfolding proceeds in two ways depending on the sign of the differential tension (Fig. S4), which can be easily understood by considering a single cell with $\alpha - \beta > (\alpha - \beta)_{th}$ [Eq. (6)] supported by the basement membrane. If $\alpha > \beta$ the cell is apically constricted at small κ and the curvature of the basement membrane is small too. As a result, an increase of κ from a infinitesimally small value to a finite value results in a slight unfolding (top row of cells in Fig. S4). On the other hand, if $\alpha < \beta$ then the cell is basally constricted at small κ , which means that the curvature of the membrane is large (bottom row of cells in Fig. S4). This is associated with a considerable membrane bending energy even with small κ meaning that the tissue unfolds more than in former case at a finite bending modulus.

This behavior is quantified by a dimensionless curvature of cells on the membrane conveniently expressed by the product of cell curvature and height, $|cl|$. In Fig. S4, $|cl|$ is plotted against membrane bending modulus κ for

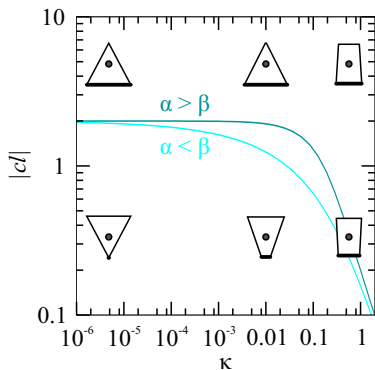


Fig. S4. Product of curvature and height in isolated cells supported by the basement membrane vs. membrane bending rigidity κ . At finite κ , basally constricted cells (cyan line; $\alpha = 0.6, \beta = 1.07$) are unfolded more than the apically constricted cells (dark blue line; $\alpha = 1.07, \beta = 0.6$). Insets show cell shapes at $\kappa = 0, 0.01$, and 1.

both $\alpha > \beta$ and $\alpha < \beta$ on a log-log scale. At very small κ $|cl| = 2$, which corresponds to apically constricted triangular cell ($cl = -2$) or basally constricted triangular cell ($cl = 2$). With increasing κ , $|cl|$ decreases faster at $\alpha < \beta$ than at $\alpha > \beta$, which means that at small κ basally constricted cells unfold more than the apically constricted cells. The asymptotic behavior of $|cl|$ for $\kappa \gg 1$ is identical in both cases.

In Fig. S5 we plot cell curvature and height (i.e., tissue thickness) as a function of differential tension $\alpha - \beta$ for three values of basement membrane bending modulus. The left panel shows the $\kappa = 0$ case where the basally constricted cell at a given $\alpha - \beta < 0$ is equivalent to the apically constricted cell at a positive differential tension of identical magnitude. This is reflected in the symmetry of cell height (cyan line) and in the antisymmetry of curvature (gray line). At a finite κ , the symmetry and the antisymmetry are absent, and at a given magnitude of differential tension $|\alpha - \beta|$ the apically constricted cells at $\alpha > \beta$ are more curved and taller than the basally constricted cells at $\alpha < \beta$.

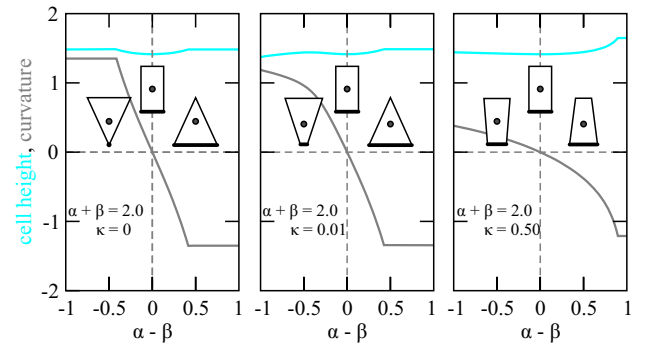


Fig. S5. Curvature and height of a cell supported by the basement membrane of $\kappa = 0, 0.01$, and 0.5 (left, middle, and right panel, respectively) plotted vs. differential tension $\alpha - \beta$. Also included are shapes of cells at $\alpha - \beta = -0.5, 0$, and 0.5.

D. Cell-cell repulsion

Yet another factor determining fold shape is the repulsion between impenetrable cells represented by a hardcore potential. Each folded morphology can be thought of consisting of two segments. The *favorable* segment contains cells whose shape is very close to that of isolated cells at given α, β , and κ so that their energy is small. On the other hand, cells in the *unfavorable* segment are deformed very much compared to isolated cells at given α, β , and κ and their energy is large. In periodic folds, both favorable and unfavorable segments are needed (Ref. [28] of the main text).

As the differential tension $\alpha - \beta$ is increased, cells in the unfavorable segment are energetically more and more costly. As a result, in the minimal-energy fold the unfavorable segment consists of as few cells as possible, lead-

ing to sharp grooves and crests (Fig. S6A). In turn, this means that neighboring grooves and crests are physically very close to the point that they actually touch so that non-neighboring cells push against each other (e.g., in waveforms with $\alpha > 2.5$ in Fig. S6A). At this stage, the contour of the waveform depends on cell-cell repulsion very much and the tissue shape becomes saturated, unable to adapt to a further increase of differential tension. Thus the compact folds are stabilized primarily by apical (or basal) constriction and hard-core cell-cell repulsion whereas the invaginated and evaginated are stabilized mainly by the bending rigidity of the basement membrane and only to a lesser degree by the repulsion between cells (Fig. S6A). In the wavy folds (Fig. 1D, E of the main text) cell-cell repulsion is irrelevant.

Including this constraint in numerical simulations is usually quite a challenge. Here we achieved this as follows: At every minimization step we run the routine which checked whether any two cell overlap. If this was the case, vertices defining both cells in question were forced to a position such that the cells touched rather than overlapped. First, the routine identifies the top and the bottom vertex of the waveform [$\mathbf{r}_{\text{top}} = (x_{\text{top}}, y_{\text{top}})$ and $\mathbf{r}_{\text{bott}} = (x_{\text{bott}}, y_{\text{bott}})$]. Next, the coordinates x_{top} and x_{bott} are used as spatial barriers. Cells that were initially on either side of the barrier are not able to cross it. Specifically, for a vertex with coordinates $\mathbf{r} = (x, y)$ the sign of the quantities $x - x_{\text{top}}$ and $x - x_{\text{bott}}$ is forced to remain unchanged during the course of simulation; here x_{top} and x_{bott} are of course updated at every minimization step.

E. Stroma

Finally, fold morphologies are only possible in an epithelium supported by a stroma that ensures a global planar nature. Here such a stroma is represented by periodic boundary conditions mimicking, e.g., an epithelium floating on a fluid-like substrate. Such a substrate can be viewed as an idealization of a small part of a droplet (Fig. S7) corresponding, e.g., to yolk in a *Drosophila* embryo without the vitelline membrane as discussed in Ref. [27] of the main text.

II. PHASE DIAGRAM OF FOLD MORPHOLOGIES

The waveforms shown in Fig. 1D, E of the main text are just a representative subset of all waveforms that we obtained. A more comprehensive selection is presented in Fig. S8, panels A and B corresponding to those in Fig. 1D and E of the main text. Figure S8 illustrates two important facts: (i) the continuous deformation of any given shape as either apical or basal tension and the basement membrane bending rigidity are varied, and (ii) the uneven sensitivity of waveforms to these parameters

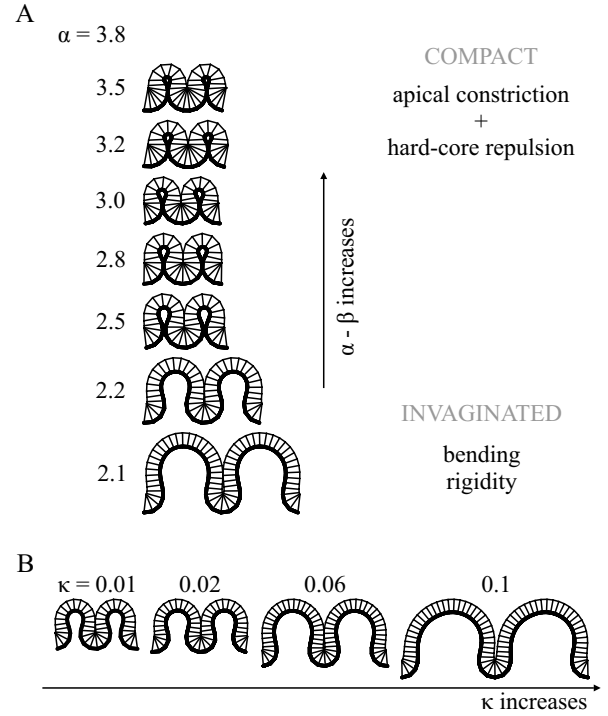


Fig. S6. Comparison of compact and invaginated folds at $\beta = 0.6$ and $\kappa = 0.02$ and various α (panel A). The shape of the former is determined mainly by apical constriction of groove cells and by the cell-cell repulsion whereas the latter are stabilized primarily by the basement membrane. Panel B shows a sequence of waveforms at $\alpha = 2.2$ and $\beta = 0.6$ as κ is increased, illustrating the ever less important role of cell-cell repulsion.

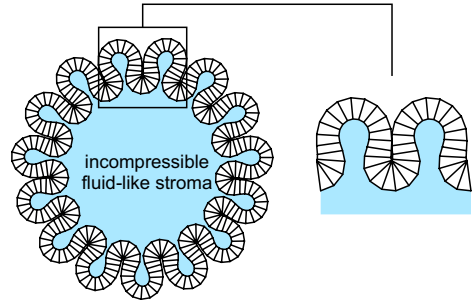


Fig. S7. Folded 2D model epithelium around an incompressible droplet of fixed area (blue). The model explored in this study can be viewed as a small part of such an epithelium.

across the phase diagram.

The leftmost columns of the two panels of Fig. S8 contain shapes at vanishing bending rigidity of the basement membrane ($\kappa = 0$). As a result, a shape with a given apical and basal tension $\alpha_A = 0.6$ and β_A in panel A is a mirror image of its counterpart with $\alpha_B = \beta_A$ and $\beta_B = 0.6$ in panel B; as the waveforms are plotted in a crest-to-crest fashion, a half-wavelength horizontal shift is needed to appreciate the correspondence. In the regime of compact folds at large differential tension (e.g., at $\beta \gtrsim 2.5$

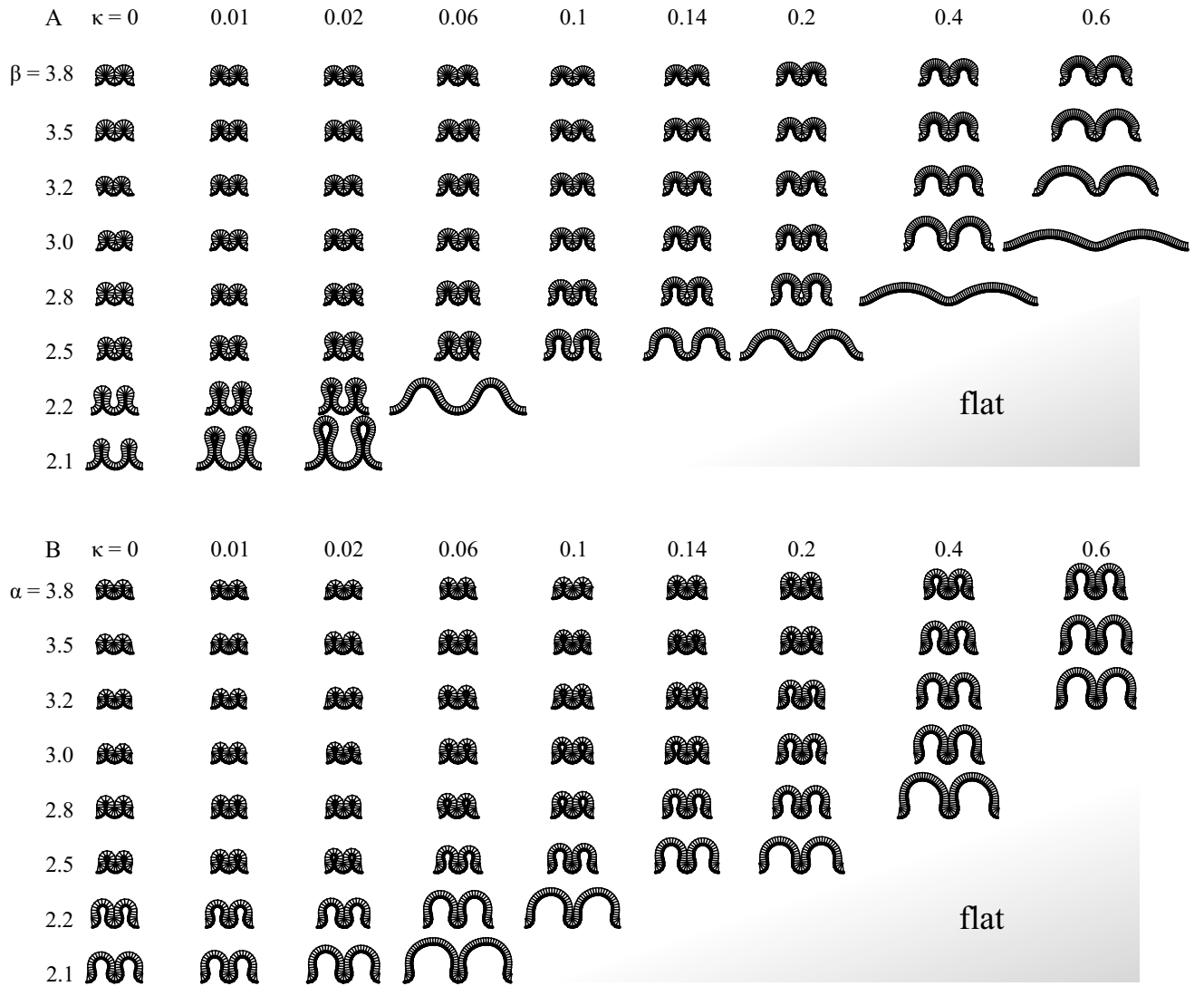


Fig. S8. Selected fold morphologies for $\alpha < \beta$ (A) and $\alpha > \beta$ (B). In panel A $\alpha = 0.6$ and in panel B $\beta = 0.6$; note that neither the bending modulus of the membrane (columns) nor the basal and apical tension (rows) is equidistant. Flat epithelia are stable at large κ and small β and α , respectively, as sketched by the shaded regions.

in panel A and $\alpha \gtrsim 2.5$ in panel B) the folds are tightly packed and rather symmetric about the horizontal, but at intermediate differential tensions the difference between the evaginated folds with basally constricted cells in the crests in panel A and the corresponding invaginated folds with apically constricted cells in the grooves in panel B is clear.

At finite κ , this symmetry is broken because the bending rigidity of the basement membrane prevents basal constrictions of the folds with in Fig. S8A because it is located at the basal side. On the other hand, waveforms in Fig. S8B may contain a certain fraction of apically constricted cells, which are located in the grooves. This asymmetry is clearly seen in the generally larger wavelength of any given fold in panel A compared to its counterpart in panel B, the most extreme manifestation of this effect being the wavy folds in panel A.

Another consequence of the basement membrane is the small range of κ where evaginated folds are stable. As evident from the waveforms in the bottom rows of both panels in Fig. S8, the basement membrane permits deep and sharp invaginations within a broad range of κ provided that the differential tension is suitable (as seen, e.g., in the $\alpha = 2.8, \kappa = 0.4$ in panel B) but tall evaginations are only possible at very small κ (cf. waveform $\beta = 2.1, \kappa = 0.02$ in panel A). Thus a sharp evagination can be viewed as a signature of a small bending rigidity of the basement membrane.

Apart from the wavelength, the main difference between folds with $\alpha < \beta$ in Fig. S8A and those with $\alpha > \beta$ in Fig. S8B is the relative tissue thickness in grooves and in crests. In waveforms in panel A, crest cells are taller than those in the grooves, and the grooves are incompletely closed or even open (the most extreme case be-

ing the wavy folds). Waveforms in panel *B* have crests which consist of trapezoidal cells shorter than cells in the grooves, which are apically constricted; as a result, the grooves are closed.

Some waveforms in Fig. S8 apparently consist of very simple geometric shapes. The contour of the meandering evaginated shape shown in Fig. 9A can be approximated by circular arcs of two radii, and the midline of the wavy fold in Fig. 9B is almost sine-like.

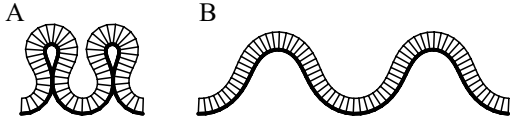


Fig. S9. Meandering evaginated fold (*A*; $\alpha = 0.6, \beta = 2.2$, and $\kappa = 0.02$), and sine-like wavy fold (*B*; $\alpha = 0.6, \beta = 2.2$, and $\kappa = 0.06$).

Figure 1*D, E* of the main text zooms in the region of the phase diagram where the differential tension is large enough so as to stabilize fold morphologies yet not too big so as to induce the reentrant fold-flat transition explored in detail in Ref. [28] of the main text. In Fig. S10, we sketch the **global topology of the phase diagram** which does contain this transition. As any finite bending rigidity of the basement membrane disfavors fold morphologies compared to either thin and the thick flat epithelium stable at small and large differential tensions, respectively, we expect that the fold region in the phase diagram should gradually shrink as κ is increased and that there exists a critical bending rigidity of the basement membrane κ_c beyond which the epithelium is flat at any α and β .

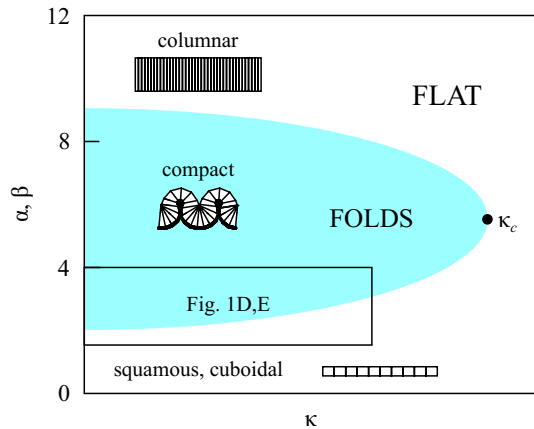


Fig. S10. Global topology of the phase diagram of fold morphologies with the reentrant flat-fold-flat morphological sequence at bending rigidities smaller than the critical value of κ_c . Also indicated semiquantitatively is the domain explored in Fig. 1*D, E* of the main text.

III. PHYSIOLOGICAL FUNCTION OF EPITHELIAL FOLDS

Monolayered epithelial sheets cover body surfaces of invertebrates and luminal surfaces of most vertebrate internal organs. Epithelial sheets with a free surface are polarized and form barriers which (i) control the passage of matter and provide (ii) protection from mechanical damage and (iii) invasion by different organisms or particles. The barrier function of epithelia depends on close lateral attachments of the cells. The shape and the distribution of cells in epithelial folds varies among the four fold types, and here we discuss the biological relevance of each type in relation to organ function and dynamics.

Compact folds with large basal tension are present in the wing imaginal disc of *Drosophila melanogaster* larva (Fig. 3*A** of the main text). Imaginal discs in holometabolous insect larva are small sacs of concentrated epithelial folds, fated to differentiate into the epidermal structures of the adult during metamorphosis. During imaginal disc formation, considerable epithelial growth and folding takes place in the small area of the sac. Folds are placed tightly close to each other (so that their wavelength is short) and most cells are constricted. Compact folds are also observed in some areas of bronchus (Fig. 3*A*** of the main text). Lung bronchi are the conducting part of respiratory system, functioning in air passage and in conditioning of the air with mucus covering the internal surface of bronchi. The bronchus epithelial folds serve to increase surface area for mucus secretion and enable changing of airway diameter, which is achieved by differential epithelial folding with compact regions.

The folded intestinal epithelium is the site for digestion and absorption of food. **Invaginated folds** of the intestine epithelium in bony fishes increase the digestive and absorptive surface area (Fig. 3*B** of the main text). In mammal colon (Fig. 3*B*** of the main text) the epithelium surface is increased by folds for effective resorption of electrolytes and water as well as for secretion of mucus. Both epithelia represent the invaginated fold type with $\alpha > \beta$ and they consist primarily of absorptive cells. The trapezoidal cells with wide apical surfaces located in the crests are shorter and wider than cells in the grooves which are constricted apically and enlarged basally. This type of epithelium functions primarily in absorption and fluid transport.

Invaginated folds with $\alpha < \beta$ are identified in actinopharynx of cnidarians, serving as the organ of water flow and food transport (Fig. 3*C** of the main text) and in vertebrate bronchiole, functioning in air conduction and lipoprotein secretion (Figs. 3*C*** and 3*C**** of the main text). In these folds, cells in the crests are basally constricted and are taller and more numerous than those located in the grooves. Grooves are wider than in the invaginated epithelium with $\alpha > \beta$ (Figs. 3*B** and 3*B*** of the main text). This type of epithelium functions primarily in secretion and in air, fluid or food

transport. Basally constricted crest cells may increase secretory activity by releasing packages of secretory vesicles with lipoprotein to prevent collapsing of bronchioles.

In a **wavy fold**, the wavelength is much larger than the amplitude. This type of epithelial folds is found at the body surface of snail *Helix sp.* (Fig. 3D* of the main text) covered by mucus-secreting epidermis. Folds increase the surface area for secretion and allow extension of body surface. The apical surfaces of epidermal cells remain fully exposed to the exterior in the crests as well as in the grooves. Wavy epithelial folds are also present in the hindgut of earthworm *Lumbricus sp.* (Fig. 3D** of the main text), functioning in resorption of water, osmoregulation, and feces formation. In vertebrate bronchiole (Fig. 3D*** of the main text) the wavy epithelium functions in air conduction and lipoprotein secretion. The fold-to-fold variability observed in histological sections reflect the dynamics of epithelial folds related to changes of lumen diameter and secretion.

Folds in the **evaginated epithelium** display wide grooves and basally constricted cells in crests which are slightly higher than cells in grooves. Evaginated folds are identified in bronchiole of cat lung (Fig. 3E* of the main text) providing air conduction. Here the folds enable lumen to expand when air or food passes through it. Evaginated epithelial folds are also found in mammal oviduct (Fig. 3E** of the main text) with bidirectional transport of the gametes and secreted fluids. The longitudinal folds in the intestine of trout (Fig. 3E*** of the main text) increases the digestive and absorptive surface area and the distinct grooves in between the folds serve in the retention of ingested food for longer periods and in nutrition passage.

IV. APPARENT DISTORTION OF FOLDS IN HISTOLOGICAL SECTIONS

None of the histological sections presented in Fig. 3 of the main text was prepared specifically for morphometrical purposes related to our theoretical findings. Instead, the sections were chosen based on qualitative agreement of the folds that they contain with our theoretical predictions summarized in Fig. S8. While studying the published sections and our own archive, we did bear in mind that the sections may not show a given morphology as representatively as possible partly due to purely geometrical reasons related to the direction of the cut while slicing the sample.

Ideally, a fold epithelium would be cut along a plane perpendicular to grooves and crests. Sectioning it at a non-ideal angle distorts the representative cross-section and thus biases the measured absolute and relative modulation of tissue curvature c and thickness l as key parameters of fold morphologies. For each theoretical fold contour, the distortion can be quantified semi-analytically as follows. We first approximate the exact contour by a two interpolating functions $\mathcal{A}(x)$ and $\mathcal{B}(x)$ representing

the apical and the basal side of the tissue, respectively. [Here we tacitly assume that there are no overhangs in the folds so that both $\mathcal{A}(x)$ and $\mathcal{B}(x)$ depend on a single coordinate x ; see Fig. S11. In case of overhangs, a more general representation is needed.] In a parametric form the apical and basal surface are thus fully described by $\mathbf{r}_a = (x, y, \mathcal{A}(x))^T$ and $\mathbf{r}_b = (x, y, \mathcal{B}(x))^T$, respectively, where the y axis points along the folds.

Cutting these surfaces in any plane given by $y = y_0$ produces a representative cross-section but rotating the cut plane does not. Here this effect is quantified by rotating the apical and basal surface relative to the cut plane, that is, about the x and the z axis by angles X and Z , respectively. These rotations are represented by matrices

$$\mathbf{R}_x(X) = \begin{pmatrix} 1 & 0 & 0 \\ 0 & \cos X & -\sin X \\ 0 & \sin X & \cos X \end{pmatrix} \quad (7)$$

and

$$\mathbf{R}_z(Z) = \begin{pmatrix} \cos Z & -\sin Z & 0 \\ \sin Z & \cos Z & 0 \\ 0 & 0 & 1 \end{pmatrix}, \quad (8)$$

After both rotations, the apical surface after the rotation around both axes is transformed to

$$\begin{aligned} \mathbf{r}'_a &= (x'_a, y'_a, z'_a)^T = \mathbf{R}_x(X)\mathbf{R}_z(Z)\mathbf{r}_a \\ &= \begin{pmatrix} x \cos Z - y \sin Z \\ -\mathcal{A}(x) \sin X + \cos X(y \cos Z + x \sin Z) \\ \mathcal{A}(x) \cos X + \sin X(y \cos Z + x \sin Z) \end{pmatrix} \end{aligned} \quad (9)$$

In the cut plane $y'_a = y_0$ which means that

$$y = [y_0 + \mathcal{A}(x) \sin X]/(\cos X \cos Z) - x \tan Z \quad (10)$$

and after a few final straightforward steps we obtain

$$\mathbf{r}'_a = \begin{pmatrix} x/\cos Z - [y_0 + \mathcal{A}(x) \sin X] \tan Z/\cos X \\ y_0 \\ [\mathcal{A}(x) + y_0 \sin X]/\cos X \end{pmatrix} \quad (11)$$

The results for the coordinates of a point at the basal surface are analogous. Without loss of generality we can set $y_0 = 0$ and plot the parametric curves $(x'_a(x), z'_a(x))$ and $(x'_b(x), z'_b(x))$ representing the apical and the basal side, respectively.

Figure S11A shows the representative cross-section of the folds, the black, dark blue, and cyan arrow indicating the true wavelength λ as well as groove and crest thicknesses l_g and l_c , respectively. If the cut plane is tilted about the x axis (Fig. S11B; here $X = 36^\circ$) the groove and the crest thicknesses are apparently increased as seen by comparing the true l_g and l_c (dark blue and cyan arrow, respectively) with the contour. The wavelength remains unchanged. Rotating the cut plane about the z axis leaves the groove and crest thicknesses unaltered but leads to an apparent increase of the wavelength (Fig. S11C; here $Z = 36^\circ$). Finally, simultaneous tilt

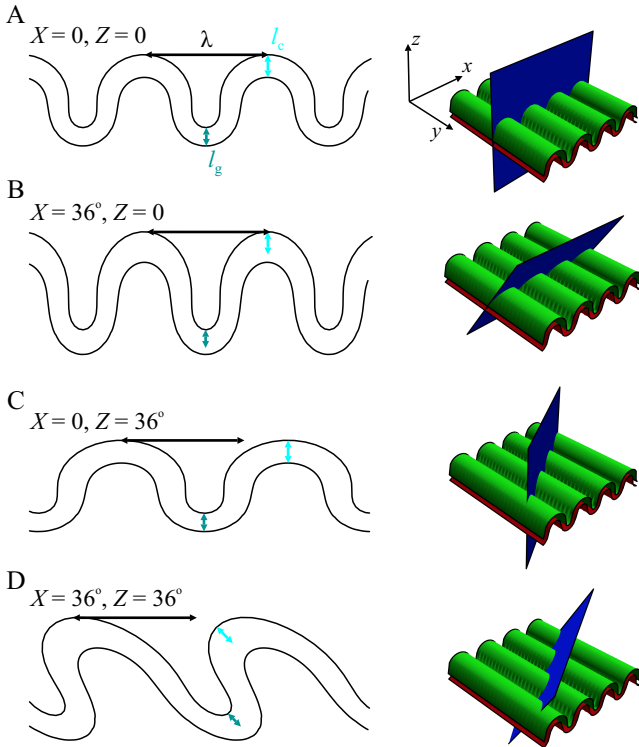


Fig. S11. Geometrical distortion of the folds caused by misalignment of the cut plane. The representative fold contour is seen in a section perpendicular to the direction of the grooves (A, arrows indicate groove and crest tissue thickness and fold wavelength). Tilting the cut plane does not affect the fold wavelength but the apparent groove and crest tissue thicknesses are increased (B); rotating it about the z axis pointing into lumen leaves the thickness unchanged but increases the wavelength (C). A combination of tilt and rotation leads to tilted folds and an apparent increase of l_g , l_c , and λ (D).

about the x axis and rotation about the z axis result in a combined distortion of the cross-section seen in Fig. S11D for $X = 36^\circ$ and $Z = 36^\circ$. In this case, the folds themselves are tilted rather than upright and they are not symmetric, λ , l_g , and l_c and all are apparently increased. Moreover, the true bottom of the groove and the true top of the crest are both displaced as indicated by the dark blue and the cyan arrow, respectively. Interpreting the apparent groove and crest thicknesses measured at the top and the bottom of the tilted and rotated section may thus be challenging.

An additional effect potentially leading to a larger error are the often poorly visible cell boundaries, which make measurements of tissue thickness even more difficult. Within our model, cells are perpendicular to tissue cross-section midline but in a tilted and histological section this may no longer hold. Thus the apparent tissue thickness measures as the perpendicular distance between the apical and the basal surface is generally different from the true distance.

We expect that in most histological sections, the ori-

entation of the cut plane is somewhat imperfect, with tilt and rotation angles of up to 10 or 15° being acceptable. In addition, the epithelium itself is almost never ideally periodic. The direction of grooves themselves may vary so that a given histological section may be representative in a part of the sample but not across all of it. These considerations must be taken into account when interpreting the sections, and it is possible that they are responsible for some fold-to-fold variability seen in Fig. 3A*-E*** of the main text.

Finally, we note that seeing a continuous albeit distorted folds in a non-representative histological section is also a strong indication that the epithelium in question indeed has longitudinal folds and not villi. Irrespective of the orientation of the cut plane, folds should always appear as a continuous contour but in case of villi one may either see a representative lengthwise cross-section or just a disconnected circular patch as in Fig. 4f in Ref. [1]. In addition, the spacing of the folds seen in Fig. 3A*-E*** of the main text is still very regular and well-defined whereas in villi it need not appear to be regular because of a misaligned cut plane even in fairly ordered villi patterns such as the hexagonal and the square lattice of the colon and the intestinal villi, respectively (Ref. [5] of the main text). An oblique-view electron micrograph of the epithelium such as that in Fig. 1A of the main text is even more convincing but seldom available.

V. MODEL PARAMETERS

The model parameters of the theoretical epithelial folds overlaid onto histological sections in Fig. 3A*-E*** of the main text are summarized in Table SI. Note that as far as fold shape is concerned, the only meaningful parameters are the reduced differential tension $\alpha - \beta$ and bending rigidity κ . As mentioned in the main text, varying α and β at fixed $\alpha - \beta$ and κ merely affects cell height-to-width ratio but not the shape of the waveform.

Table SI. Model parameters of the theoretical folds shown in panels A*-E*** of Fig. 3 of the main text.

tissue	α	β	$\alpha - \beta$	κ
fruit fly wing imaginal disc, A*	0.6	2.8	-2.2	0.01
cat lung bronchus, A**	0.6	2.8	-2.2	0.01
silver sailfin molly intestine, B*	2.1	0.6	1.5	0.02
rat small intestine, B**	3.8	0.6	3.2	0.4
metridium actinopharynx, C*	0.6	2.8	-2.2	0.14
cow bronchus, C**	0.6	2.5	-1.9	0.1
mouse bronchiole, C***	0.6	2.5	-1.9	0.1
snail body surface, D*	0.6	3.2	-2.6	0.6
earthworm hindgut, D**	0.6	2.8	-2.2	0.4
mouse bronchiole, D***	0.6	2.8	-2.2	0.3
cat lung bronchus, E*	0.6	2.1	-1.5	0.002
monkey oviduct, E**	0.6	2.1	-1.5	0.002
trout intestine, E***	0.6	2.3	-1.7	0

-
- [1] Yao J, Maslov KI, Puckett ER, Rowland KJ, Warner BW, Wang LV (2012) Double-illumination photoacoustic microscopy. *Opt Lett* 37:659-661.